Dislocations at coalescence boundaries in heteroepitaxial GaN/sapphire studied after the epitaxial layer has completely coalesced

T.J. O'Hanlon, T. Zhu, F.C.-P. Massabuau, R.A. Oliver*

Department of Materials Science and Metallurgy, University of Cambridge, 27 Charles Babbage Road,
5 Cambridge CB3 0FS, UK

Abstract

We have performed cross-sectional scanning capacitance microscopy (SCM), cathodoluminescence (CL) microscopy in the scanning electron microscope (SEM) and transmission electron microscopy
10 (TEM) all on the same few-micron region of a GaN/sapphire sample. To achieve this, it was necessary to develop a process flow which allowed the same features viewed in a cleaved cross-section to be traced from one microscope to the next and to adapt the focused ion beam preparation of the TEM lamella to allow preparation of a site-specific sample on a pre-cleaved cross-section. Growth of our GaN/sapphire samples involved coalescence of three-dimensional islands to form a continuous film.
15 Highly doped marker layers were included in the sample so that coalescence boundaries formed late in the film growth process could be identified in SCM and CL. Using TEM, we then identified one or more dislocations associated with each of several such late-coalescing boundaries. In contrast, previous studies have addressed coalescence boundaries formed earlier in the growth process and have shown that early-stage island coalescence does not lead to dislocation formation.
20

Introduction

The growth of gallium nitride (GaN) on sapphire remains the most common approach to achieve the high quality epitaxial layers required for the fabrication of blue and green light emitting diodes (LEDs). Threading dislocations are ubiquitous in these heteroepitaxial layers, and can have
25 deleterious impacts on the performance of not only LEDs but also electronic devices[1]. However, their generation mechanism is not fully understood. In general, where heteroepitaxial growth involves a fairly small lattice mismatch (up to about 4 or 5%), threading dislocations may be introduced into a growing film once a critical thickness has been exceeded; they are required to allow the glide of misfit dislocation segments from the surface to the interface between the heteroepitaxial layer and

* To whom correspondence may be addressed: rao28@cam.ac.uk

This is a peer-reviewed, accepted author manuscript of the following article: O'Hanlon, T. J., Zhu, T., Massabuau, FC-P., & Oliver, R. A. (2021). Dislocations at coalescence boundaries in heteroepitaxial GaN/sapphire studied after the epitaxial layer has completely coalesced. Ultramicroscopy, 231, [113258]. https://doi.org/10.1016/j.ultramic.2021.113258

the substrate in order to relieve strain[2,3]. However, the large lattice mismatch between GaN and sapphire (≈16% at room temperature[4]) results in an array of geometrically necessary misfit dislocations at the GaN/sapphire interface[5]. These are present from the very beginning of the growth of the epitaxial layer and accommodate the vast majority of the mismatch. The remainder of the lattice mismatch is manifested as elastic strain. Hence, although threading dislocations in GaN/sapphire may form as a *consequence* of the large mismatch, if the dislocation line vector is perpendicular to the GaN/sapphire interface they do not relieve the strain and their formation is not driven by strain relief considerations.

Instead, Ning et al.[5] suggested dislocations may be generated by the coalescence of three dimensional islands formed during growth which have a small relative misorientation, yielding a very low angle grain boundary. If the islands have a relative rotation about the [0001] axis, a pure tilt boundary will be generated, accommodated by edge *a*-type TDs with Burgers vector, ***b***, parallel to $\langle 11\bar{2}0 \rangle$. Rotation about an in-plane direction would yield a pure twist boundary with screw *c*-type dislocations (**b** parallel to $\langle 0001 \rangle$). Coalescing islands with both tilt and twist misorientation would generate mixed (*a*+*c*)-type dislocations. The observation of arrays of threading edge dislocations in fully coalesced films by transmission electron microscopy (TEM) was considered to be evidence for the formation of such very low angle grain boundaries. However, studies on partially coalesced films by TEM[6] and atomic force microscopy (AFM)[7] failed to find any preferential occurrence of dislocations at boundary locations. Furthermore, Moram *et al.* showed that threading dislocations can migrate into arrays by vacancy-assisted climb to minimise in-plane stresses[8]. Hence, the observation of dislocation arrays is not necessarily evidence that such arrays formed by island coalescence.

Earlier studies which attempted to directly link coalescence boundary locations to dislocation generation used the morphology of a partially coalesced layer to indicate the positions of the coalescence boundaries, and therefore tended to focus on the early stages of the coalescence where separate islands could be easily identified. Once three-dimensional islands have fully coalesced to form a two-dimensional layer no topographic signature remains. However, Oliver[9] showed that it is possible, employing scanning capacitance microscopy (SCM), to use highly doped marker layers to track the progression of island coalescence in fully coalesced films. The results of that study showed that even when the majority of islands in a film coalesce during the early stages of growth, some regions of incomplete coalescence may remain where islands coalesce more slowly, in the later stages of growth. Here, we demonstrate an approach to identifying such *late coalescing boundaries* and preparing site-specific lamellae for TEM at the relevant locations. We then use the methods we have developed to investigate whether dislocation locations correlate with the locations of these atypical boundaries.

65 Our study is an example of an approach to micro- and nano-characterisation which allows the examination of the same feature in multiple different microscopes. This is sometimes termed "correlative microscopy" or alternatively "multi-microscopy"[10,11]. The key goal of this approach is to enable a direct correlation between the structure and properties of a specific object, to allow a more complete understanding of their interrelationship than the more statistical approach achieved by
70 looking at separate subsets of a population of structures with different techniques. It has been powerfully applied to defects in the nitrides in the past by Massabuau *et al.*[10,12] and Mancini *et al.*[11] For example, Massabuau *et al.* combined morphological measurements in AFM, with optical property measurements from cathodoluminescence (CL) and defect analysis and compositional mapping in TEM to elucidate the impact of strain field interactions between dislocations on their optical
75 properties[12]. Here, we expand on the range of techniques which have previously been used in multi-microscopy analyses of nitrides, bringing in the electrical characterisation capability of scanning probe microscopy by using SCM as a tool for coalescence boundary identification.

Experimental methods

80 **Sample Growth**

The growth of GaN on sapphire involving the coalescence of three dimensional (3D) islands to form a two dimensional (2D) film is often referred to as 3D-2D growth. Oliver[9] described the incorporation of highly doped marker layers which allow tracking of the island coalescence in a 3D-2D growth process, and a very similar growth routine was followed here. The details of the growth process may
85 be found in reference 9. Briefly, the sapphire substrate was initially annealed in NH_3. At the end of this anneal step an additional flux of SiH_4 was added to form a SiN_x nanomask on the sapphire surface, an approach sometimes referred to as micro epitaxial layer overgrowth (microELOG). The temperature was then reduced to 540 °C for the growth of a 50 nm low temperature GaN nucleation layer (NL). The NL was annealed at 1020 °C after growth in order to encourage 3D island formation,
90 and the GaN growth thereafter commenced at a reduced temperature (980 °C) and V:III ratio to encourage 3D growth. As the growth progressed, both the V:III ratio and the temperature were increased to enable island coalescence and a transition to 2D growth. Highly doped marker layers (consisting of approximately 100 nm of GaN doped to 1×10^{19} cm^{-3} with Si) were introduced after the first ~1000 nm of growth and thereafter after every 750 nm of growth. No intentional dopant flux
95 was used between the marker layers, but earlier studies show that during coalescence, where semi-polar facets are present on 3D islands, these facets have an enhanced incorporation rate for unintentional dopants, particularly oxygen[13]. This approach results in samples with a dislocation density of $3 - 6 \times 10^{8}$ cm^{-2}.

100 **Multi-microscopy**

Coalescence boundary positions on samples containing marker layers have previously been located using SCM[9], a technique based on AFM in which the change in capacitance with voltage occurring upon application of an alternating bias is used to reveal variations in carrier density within a semiconductor sample[14]. In GaN, preparation of samples for cross-sectional SCM analysis is typically
105 achieved by cleaving, since polishing and ion-milling can very significantly degrade the achievable SCM signal[15]. However, whilst SCM is useful for the identification of marker layers and hence coalescence boundary locations in our samples, it cannot unambiguously reveal the presence of dislocations near to the cross-sectioned surface, and it provides no access to the Burgers vector of such dislocations. The most appropriate technique for such cross-sectional dislocation analysis is
110 TEM, but basic TEM techniques cannot conveniently reveal the location of the doped layers which mark the coalescence boundaries, and the small sampling volume in TEM is not suited to the broad cross-sectional areas which must be sampled to locate boundaries which were late to coalesce. Combining SCM and TEM to first identify the coalescence boundary location and then investigate the defects located at that boundary required the development of a new process flow for the
115 preparation of samples, facilitating the application of both microscopy techniques in series.

Here, our multi-microscopy analysis begins with CL imaging in the scanning electron microscope (SEM). Room temperature SEM-CL images were taken on a Philips (now Thermo Fisher Scientific) XL30 field emission SEM operating at 3 kV using a Gatan MonoCL4 CL system operating in panchromatic mode. We will illustrate below that changes in dopant concentration lead to changes
120 in CL intensity, consistent with the work of Schubert *et al.* who showed that near band-edge photoluminescence increases in GaN as doping density increases[16]. CL measurements were used to help locate promising regions for SCM. Thereafter, a Veeco Dimension 3100 AFM with a Veeco SCM module and platinum-iridium coated tips (Bruker SCM-PIC) was used for open-loop SCM imaging of the marker layers to identify the positions of coalescence boundaries. Finally, TEM was performed on
125 a JEOL 4000EX operating at 400 kV.

To identify the coalescence boundaries and track them through these microscopy measurements, the following sample preparation protocol was used (which is illustrated in Figure 1): Lithographic markers were defined on the wafer surface before cleaving. A layer of photoresist (Microposit S1828) of target thickness 2 – 3 µm was spin-coated onto the sample surface and patterned into
130 stripes 10 µm wide separated by 5 µm wide windows lying parallel to one of the principal in plane directions. For the samples displayed in this manuscript the stripes were parallel to the $[1\bar{1}00]$ direction. First titanium and then gold were evaporated onto the patterned surface, forming a

metallic layer approximately 100 nm thick. The patterned sample was then cleaved to produce a cross-section perpendicular to the stripes, using the method described by Sumner *et al*.[15]

135 On the cleaved cross-section, the thick resist stripes can be seen in either SEM or the optical microscope attached to the AFM, looking like the crenellations on a medieval castle. By counting stripes from a macroscopic feature, such as the end of the cross-section, specific regions of the sample identified in SEM as having promising boundary features could then be imaged in SCM, with the pattern of cleavage steps within the identified region of the cross-section being used for final

140 location adjustments.

Sample preparation for TEM was then carried out in an FEI (now Thermo Fisher Scientific) Helios NanoLab focused ion beam scanning electron microscope (FIB-SEM). Photoresists are highly susceptible to beam damage[17] and may act as a source of organic contamination or cause outgassing problems in the TEM. In addition, the large photoresist thickness of the marker stripes may interfere

145 with uniform thinning of a lamella if the feature of interest is near the edge of a stripe (via the 'curtaining' effect[18]), or act as a weak point for failure if present in the final lamella. To avoid these issues, the stripes of photoresist were removed by soaking in acetone, leaving metal stripes in a negative pattern. These much thinner markers could still be seen in FIB-SEM by tilting the microscope stage, as indicated in Figure 2(b).

150

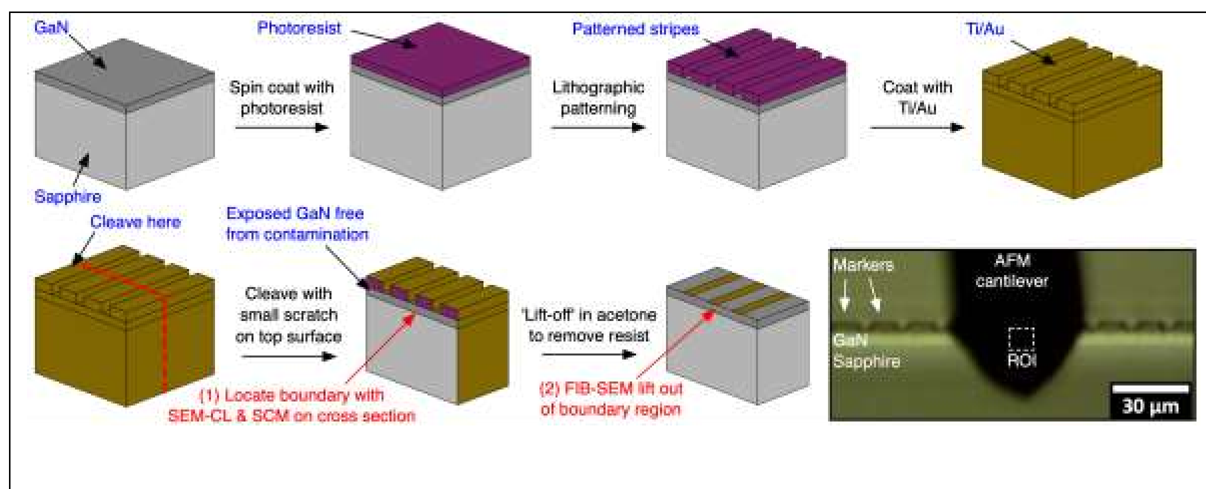

Figure 1: Schematic flow diagram of the thick lithographic marker fabrication process, and their use in correlated imaging. Inset: the markers as seen in the AFM optical microscope of a cleaved cross-section.

SCM experiments only probe a few tens of nanometres below the exposed sample surface[19]. Hence, to allow direct correlation between the SCM data and the TEM, the standard in situ lift-out procedure for preparing cross-sectional lamellae (well illustrated by Schaffer *et al.*[20]) needed

155 adaptation to allow the lamella to be prepared from an already exposed cross-section without

damaging the uncovered material. In this modified workflow, a previously characterised, late-coalescing boundary region is milled free from the from the edge of the sample from the bulk side (the 'FIB-milled side'), transferred to a TEM half-grid and thinned to electron transparency without directly exposing the 'cleaved side' to the ion beam at any stage of the process. Single-sided milling
160 is commonly used in slice-and-view FIB serial section tomography (most commonly on bulk samples[21] but also on exposed particles[22]) where only one (progressively milled) face is being investigated. It has also been demonstrated in the preparation of TEM samples[23], using a protective, removable capping object and barriers of deposited platinum to protect the top surface of a plan-view TEM lamella during lift out and thinning of the underside face. In the method presented below, in
165 contrast, the cleaved cross-sectional face is protected simply by tilting the stage to shadow the cleaved side from the ion beam.

Deposition of the protective platinum strap and milling of the adjacent stepped trench[18] were conducted with the incident ion beam offset by 5° from the surface normal, towards the FIB-milled side (a stage tilt of 47° in this instrument). The geometry of the ion beam relative to the cleaved side
170 and FIB-milled side is shown in Figure 2(a). The effect of this tilt can be seen by comparing the damage to the exposed cross-sections seen in secondary electron contrast in Figure 2(c) (at 52° tilt) and Figure 2(d) (at 47° tilt) – at a tilt of 52° the upper portion of the cross-sectional face is unintentionally milled by the ion beam, whereas at 47° the surface steps appear preserved. Figures 2(b) and 2(d) are of the same region of interest (with the metal stripes and surface steps used to
175 locate the previously characterised material seen in Figure 2(b)) while Figure 2(c) shows the unintentional milling damage on another GaN on sapphire sample.

The U-shaped undercut was milled at a 7° tilt and the micromanipulator lift-out and attachment of the lamella to a TEM half-grid with deposited platinum performed at 0° stage tilt as normal, again avoiding any direct exposure of the ion beam to the previously examined, cleaved cross-section. The
180 mounted lamella was then thinned down to the desired thickness from the FIB-milled side only, reducing the ion beam current from approximately 1 nA to 30 pA as the thinning progressed, until the desired thickness was reached. As with standard lift-out samples, the stage tilt was moved closer to 52° (i.e. parallel to the lamella's sides) as the lamella grew thinner. However, as the cleaved side had to be protected from the ion beam, a small offset angle was still maintained. Viewing the lamella
185 from above with the electron beam helped to ascertain the level of acceptable reduction in offset angle without the cleaved surface being exposed. Representative preparation parameters are given in supplementary section S-1. In protecting the exposed surface of interest, lamellae prepared by this method are necessarily slightly wedge shaped: thicker near the platinum coating and thinner towards the substrate, so care must be taken to avoid milling away the substrate-epilayer interface. Lastly,

190 the final low kV cleaning stage was carried out at with a 5 kV, 47 pA ion beam at a glancing angle of 7° to the FIB-milled face, reducing the damage layer thickness.

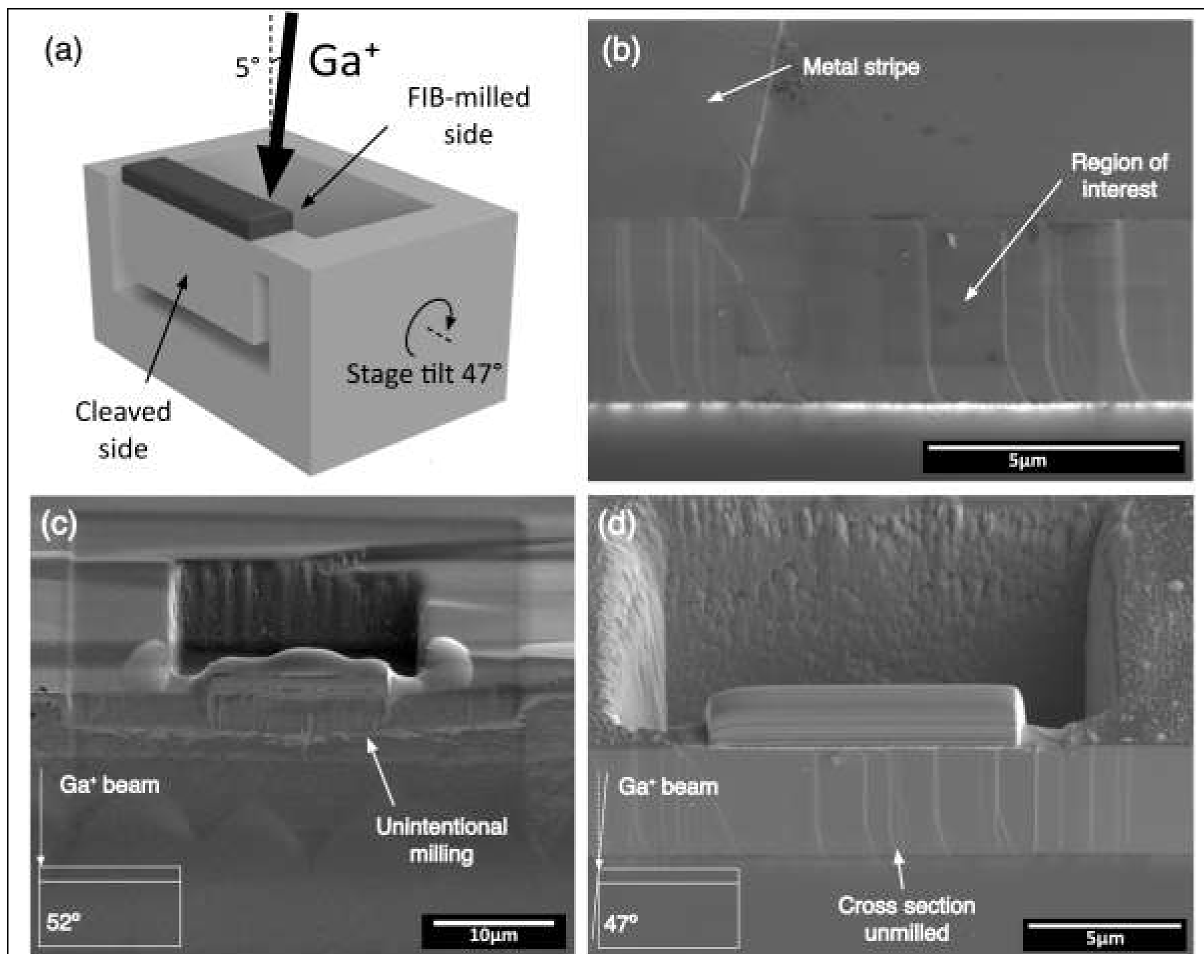

Figure 2: The edge on FIB lift-out process is illustrated schematically in (a) with the geometry of the offset ion beam relative to the cleaved and milled sides of the lamella shown. A previously identified cleaved region is shown in the secondary electron image in (b), relocated in the FIB-SEM using the metal stripe markers on the top surface and cleavage steps on the GaN cross-section. Examples of the difference in damage to the exposed cleaved cross-section when milling GaN at a stage tilt of 52° (no offset) and 47° (5° offset) are shown in (c) and (d) respectively. While the cross section in (c) is clearly unintentionally milled, this is not seen when comparing the surface steps identified prior to milling in (b) with those in (d) after milling the trench at 47° tilt.

Typical lamellae prepared for the correlative imaging in this study were thinned less than is usual for
195 GaN samples to avoid milling away any dislocations present at coalescence boundaries – the final lamella thickness was usually roughly 200 nm. However, for thinner samples, this approach can produce a lamella suitable for conventional high-resolution lattice contrast TEM imaging (an example of which is presented in the supplementary section S-2), providing evidence of the broader

effectiveness of this method. Relative to the standard lift-out procedure, FIB-induced damage to the
200 sample, such as surface amorphisation, is reduced, because only one of the two sample surfaces is
directly exposed to the ion beam rather than two.

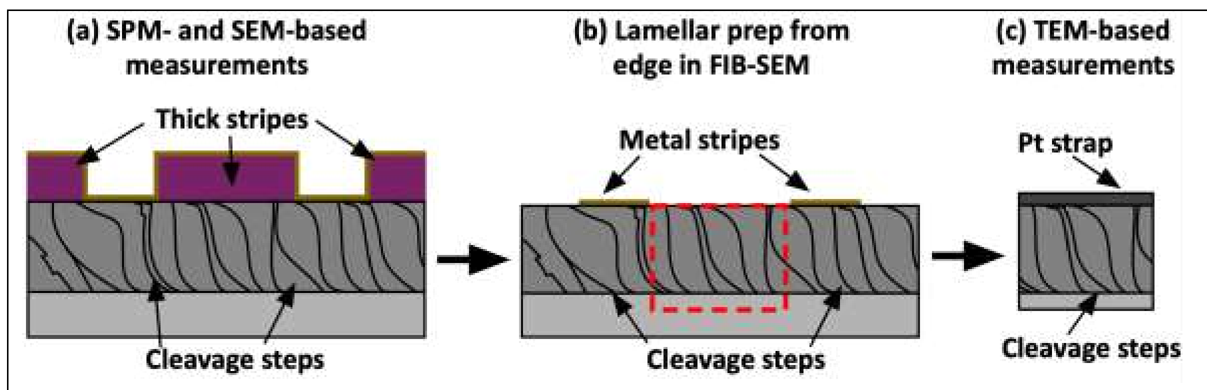

Figure 3: Schematic of the multi-microscopy workflow, indicating the different correlation features used to locate a site of interest between microscopes, with thick lithographic markers and metal stripes used for coarse location and surface cleavage steps used for more precise correlation once the approximate region had been relocated.

The full multi-microscopy workflow on a prepared cross-sectional sample, and the different
205 techniques and correlative features used at each step, are illustrated in Figure 3 and summarised
below. Firstly, the sites of interest (here late-coalescing boundaries) are identified by scanning across
cleaved cross-sections (prepared as in Figure 1 and mounted with the cross-section side pointing
upwards) using SEM-CL (allowing broad areas to be investigated more quickly) and scanning probe
microscopy (SPM) techniques (here using SCM for more precise location of a late-forming boundary).
210 The thick photoresist stripes shown in Figure 3(a) are used to identify the region of interest's location
on the sample cross-section (in the SEM-CL or the SCM's optical microscope) and relocate the area
between the two instruments (counting along from the cleave-initiating scribe mark or sample edge)
with the surface cleavage steps on the cross-section used for fine alignment. Next, the photoresist
stripes are removed (in acetone) and the sample transferred to the FIB-SEM, now mounted with the
215 striped top surface facing upwards. The metal stripes in the gaps between the photoresist remain as
the negative image of the thick stripes, and are used to relocate the desired region in the FIB-SEM,
with the surface steps on the cross-section again used for fine relocation (as shown in Figure 3(b)).
The boundary region can then be lifted out as a TEM lamella from the sample edge as described
above. Finally, the distance along the lamella and the surface step thickness contrast in the TEM can
220 be used to locate the boundary region for investigation by diffraction contrast TEM (Figure 3(c)).

Results and analysis

Using the multi-microscopy protocol described above, 6 coalescence boundaries were identified using a combination of SEM-CL and SCM, and were successfully prepared for TEM and imaged to identify their defect content. An example of a complete multi-microscopy data set is shown in Figure 225 4.

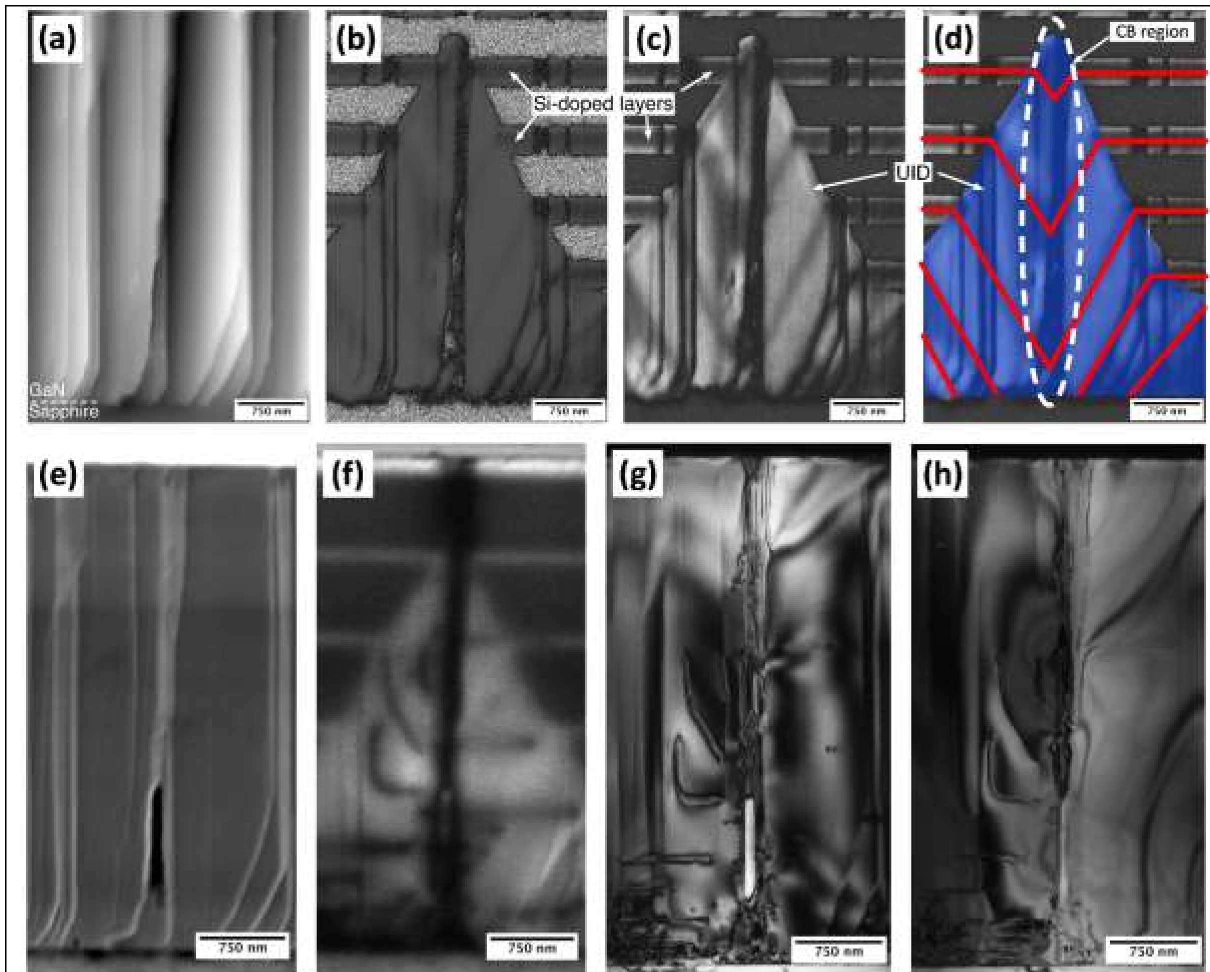

Figure 4: Directly correlated SCM, SEM-CL and TEM data from the same coalescence boundary region. (a), (b) and (c) show the height, SCM phase and SCM amplitude data respectively for SCM. The image z-height in (a) is 86 nm and the silicon-doped marker layers and the unintentionally doped region (UID - where dopants incorporate on the inclined facets) are labelled in the SCM images. The UID material is shaded in blue on the SCM amplitude data in (d) and the doped marker layer positions are marked in red, revealing the boundary region where the islands coalesced (highlighted in white). (e) and (f) show the secondary electron and panchromatic CL images in SEM-CL. Finally, bright field diffraction contrast TEM images with **g** = 0002, (g), and **g** = $11\bar{2}0$, (h), are shown, taken close to the <$1\bar{1}00$> zone axis.

Figure 4(a) shows the morphology of the cleaved surface of the sample in contact mode AFM. Steps tens of nanometres high are seen, with flat areas in between them. A small portion of the sapphire
230 substrate is seen at the bottom of the image. These data were recorded simultaneously with the data in Figure 4(b) and 4(c) which show phase and amplitude data from SCM respectively. In the SCM phase data, material in which the carrier concentration is too low for detection appears grey and noisy, since the signal exhibits no fixed phase relative to the drive phase. On the left and right sides of the image, grey noisy bands alternate with black bands, which are the n-doped marker layers. In
235 the middle of the image, a triangular black region arises at the position of a coalescence boundary. This also indicates the presence of n-type material. In the SCM amplitude image (Figure 4(c)), we can see the marker layers as darker stripes running through a brighter triangle in this region. This is because the intentionally doped marker layers have a higher carrier concentration than the surrounding material, which leads to a lower signal in open-loop SCM[24]. The marker layers bend
240 towards the GaN/sapphire interface, outlining the shape of coalescing facetted islands which were present in this region during growth; the marker layer positions are highlighted in Figure 4(d) in red, and the boundary region where the layers show the coalescing islands meeting indicated in white. The additional doped material in this region (shaded in blue in Figure 4(d)) arises from the higher unintentional impurity incorporation occurring on inclined facets as has previously been discussed by
245 Oliver and Zhu[13]. In the SCM phase image (Figure 4(b)) the marker layers cannot be readily distinguished from the unintentionally doped material because both are n-type and yield a similar signal phase. It should be noted that in both Figure 4(b) and Figure 4(c), the locations of cleavage steps can be detected in the SCM images. This arises from the change in tip-sample contact areas at a step, and hence the resulting vertical bands in the image cannot be interpreted as relating to local
250 changes in the carrier concentration.

For comparison, Figure 4(e) and 4(f) show the same region in SEM and CL respectively. The same pattern of terraces can be seen in Figure 4(a) and Figure 4(e), but Figure 4(e) reveals the presence of a void in the sample, which was not readily visible in AFM, presumably because the sample geometry prevented the tip from penetrating into it. In Figure 4(e), which is a secondary electron image, no
255 contrast is visible from the marker layers. However, in secondary electron imaging in the FIB-SEM, weak secondary electron contrast associated with the markers layers was sometimes visible. Figure 4(f) shows contrast between the doped marker layers and the surrounding undoped material at the sides of the image. However, as in Figure 4(b), the contrast at the centre of the image is dominated by the triangular region, indicating the presence of unintentional doping on inclined facets; little or
260 no contrast can be seen between the unintentionally doped triangle and the intentionally doped marker layers. This suggests that where highly doped markers layers are to be used to track the influence of sample morphology on unintentional doping, SCM may be a more powerful approach

than CL or secondary electron imaging. Nevertheless, both techniques show contrast which allow us to identify the presence of a coalescence boundary in this region. All but the uppermost highly-doped marker layer are distorted, and the unintentionally doped region extends, at the thickest point, more than 80% of the way through the layer. Typically, the unintentionally doped layer in samples grown using the method employed here is only approximately 1 µm thick. All these observations show that we have identified here a *late coalescing boundary*. As we explained in the introduction, previous experiments have not been able to examine the defect structure at such late coalescing boundaries.

In the CL data (Figure 4(f)), we also see a broad dark band passing through the apex of the unintentionally doped triangle, and other narrower dark lines emanating either horizontally or diagonally from the broad dark line. Since dislocations act as non-radiative centres in GaN, it is possible that these dark lines relate to dislocations, but they cannot be identified unambiguously from CL data alone. It should be noted that although the broad dark band is at a cleavage step, other cleavage steps do not lead to dark contrast in the CL, so this contrast is unlikely to be step-related. Using the FIB-based sample preparation process outlined above, this region was prepared into a TEM lamella. As noted above, it was deliberately only thinned to approximately 200 nm to help ensure any defects present in the boundary region were contained in the final lamella. It should be noted that where arrays of edge dislocations are observed at GaN surfaces, which are sometimes attributed to coalescence boundaries, the spacing between dislocations is typically 100 – 200 nm, so dislocations could be missed by a very thin lamella. Following thinning, the top of the sample was thicker than the bottom. Bright field diffraction contrast TEM images are shown in Figures 4(g) and 4(h), close to the $\langle 1\bar{1}00 \rangle$ zone axis. The positions of cleavage steps can be seen in the image, and compared to the cleavage steps in Figures 4(a) and 4(e). If necessary, this approach can be used to identify the position of the coalescence boundary. However, in this case, the boundary position is marked by the position of the void seen in Figure 4(e) and in the TEM data. Dislocations can be seen propagating vertically from the top of this void. Bending of the lamella from the substrate to the original epilayer surface made it impossible to get the full thickness of the film on axis simultaneously for two-beam imaging. Hence, dislocations move in and out of contrast through the image. This issue, coupled with projection issues and contrast related to foil thickness variations associated with topographic steps, makes it difficult to gauge the number of dislocations seen with absolute certainty. The presence of dislocations at this late coalescing boundary is, however, unmistakable. Figure 4(g) and 4(h) are taken in the **g** = 0002 and **g** = $11\bar{2}0$ conditions respectively (as far as was possible given the issues with lamella bending described above). Within the limitations of the analysis imposed by the lamella bending, the fact that some of the dislocations running vertically up the boundary are out of contrast in the **g** = $11\bar{2}0$ condition suggests that they are predominately *c*-

type (**b** = 0001, therefore **g**.**b** = 0)[25]. There may be some vertical features in contrast in both the **g** = 0002 and **g** = $11\bar{2}0$ image which would imply the presence of one or more (*a*+*c*)-type dislocations. (*a*+*c*) dislocations are also visible to the left of the boundary in the TEM images, running either parallel to the GaN/sapphire interface or at an angle of less than 90° to it. These correlate exactly with thinner dark lines in the CL image in Figure 4(f), confirming the dark lines seen in CL signal are attributable to dislocations. Where such dislocations run parallel to the GaN sapphire interface, they may relate to dislocations threading from the interface which turn over as a consequence of 3D island growth, and may terminate at the void associated with the boundary or annihilate with other horizontally propagating dislocations. Where these dislocations result in segments which thread vertically above the void associated with boundary, however, it is more likely that the defects originate *from* the boundary. It should also be noted that the void associated with the boundary is observed to close up within approximately 1.4 µm of the GaN/sapphire interface in both the SEM and the TEM data, so that the majority of the broad dark band in the CL which runs all the way from the interface to the GaN surface is unlikely to be related to the interaction of the electron beam with the void, and more likely to be due to the bundle of dislocations at the coalescence boundary. Overall, although the defect structure observed here is complex, it is evident that there are defects present in the region identified as a late coalescing boundary. However, this could be a coincidence. The density of defects does vary across the sample. Hence, 5 other late-coalescing boundaries were analysed using a similar multi-microscopy approach. In each case, evidence of dislocations coinciding with the boundary region was observed. The dislocation density of a sample grown under identical conditions was measured by AFM to be $(6 \pm 2) \times 10^8$ cm^{-2}. Based on data in Figure 4(c), we can identify the location of the coalescence boundary across the sample cross-section within 250 nm. Defining the coalescence boundary region then as a column through the film thickness of width 250 nm and depth 200 nm (the TEM lamella thickness), then the area at the GaN epilayer surface associated with the coalescence boundary is 0.05 μm^2. Assuming the dislocations are randomly distributed above the surface, the number of dislocations expected to intersect the surface in this coalescence boundary area is 0.3 ± 0.1. If the dislocation positions can be treated as independent to a first approximation (ignoring for example the formation of dislocation arrays via dislocation motion during growth[8]) then the distribution of the number of dislocations found in a coalescence boundary area will be Poissonian with $\lambda = 0.3$. (λ is the expected number of occurrences of a dislocation in a single coalescence boundary area). Using the Poisson distribution, the probability of finding one or more dislocations in a coalescence boundary area is then found to be 0.26. In total, 6 boundaries were investigated. The probability of finding at least one dislocation in every boundary region by chance, assuming dislocations are independent, is $0.26^6 = 0.00031$, i.e. less than 0.1%. This suggests it is very unlikely that the observed dislocations are found at the late-coalescing boundary locations

as a result of random chance, and suggests that they are indeed associated with the final part of the island coalescence process.

335

Discussion

As we discussed in the introduction, threading dislocations in GaN epilayers were originally suggested to arise from the coalescence of misoriented islands[5,26]. Investigations of this hypothesis focusing on the early stages of coalescence found no evidence of dislocations at coalescence
340 boundaries[6,7,27,28]. In contrast, we show here that boundaries arising at the very end of the coalescence process do result in the generation of threading dislocations. The differences between "early-coalescing" and "late-coalescing" boundaries are thus worthy of discussion.
For the 3D-2D sample growth method employed here, a self-assembled SiN_x nanomask is first deposited on the sapphire surface. A low temperature GaN nucleation layer is deposited, and upon
345 annealing 3D islands form in randomly-occurring gaps in the SiN_x. Matsubara *et al.*[29] studied the grain twist distribution in the as-grown nucleation layer and showed, using fast Fourier transform (FFT) analysis of high-resolution TEM images, that grains in the NL are more likely to be well-oriented relative to their near neighbours and less likely to be well-oriented relative to islands which are further away. Their study was performed on unannealed nucleation layers, and annealing may alter
350 the orientation distribution. However, assuming these results are relevant to annealed NLs, they would suggest that where regions originally nucleating far apart coalesce (as in late coalescing boundaries) they are more likely to be significantly misoriented, potentially leading to threading dislocation formation.
Studies of the early stages of coalescence suggest that larger, well-aligned islands overgrow smaller,
355 more misoriented islands[7,28], and that the dislocations in the smaller islands may turn over and annihilate one another rather than propagating. Where large, late-coalescing islands meet, they are unlikely to be able to overgrow one another. Also, additional strain may have been introduced in the separate large islands during earlier overgrowth of smaller islands.
Overall, late coalescing boundaries may need to accommodate greater misorientation than their
360 earlier-coalescing counterparts, making the introduction of TDs necessary. Whilst the formation of TDs at low angle tilt/twist boundaries is a controversial concept in 3D/2D growth, it has been widely observed at the coalescence of wing regions in epitaxial lateral overgrowth (ELOG)[30] and the void observed in Figure 4 appears reminiscent of similar voids seen in ELOG samples.
It should, however, be noted that the density of these late coalescing boundaries is low, as can be
365 seen from the wide area SCM scans of samples with marker layers presented by Oliver[9]. The evidence presented by Oliver *et al.* and Narayanan *et al.* suggests that the majority of coalescence

events occurring at an earlier stage in the growth do not lead to the formation of TDs, and that the majority of dislocations are not associated with coalescence events[6,7,28]. This may imply that the origins of the majority of threading dislocations are, as Narayanan *et al.* suggested, related to either
370 planar defects formed during low temperature growth of the nucleation layer or point defects incorporated into layers during growth. Nonetheless, these late coalescing boundaries may have a disproportionate impact on devices grown on 3D-2D GaN templates on sapphire. As shown in Figure 4, late coalescing boundaries can result in both dislocation clusters and voids. Usami *et al.*[31] have shown examples of atypical dislocations with open cores in GaN/sapphire p-n diodes both severely
375 disrupting the growth morphology and also leading to leakage pathways through the device. Hence, optimization of the growth conditions in the final stages of coalescence, may be important to avoiding "killer defects" in electronic devices for example.

Conclusion

We have demonstrated a method for the location and preparation of site-specific TEM lamellae from
380 sites already identified on cleaved cross-sections. This method is broadly applicable to any situation where a TEM sample needs to be prepared at or very close to a pre-existing cross-section or other edge. Here, we have used it to prepare TEM lamellae from regions identified in SCM and CL to contain coalescence boundaries which formed late in the growth of a GaN epilayer on sapphire by a 3D/2D method. We show that these late-coalescing boundaries are associated with one or more
385 dislocations. Coalescence boundaries formed earlier in the growth process have previously been shown not to be a source of dislocations. The late-coalescing boundaries may need to accommodate greater misorientation than those formed at earlier stages of growth, which may account for this difference. Whilst the dislocations arising from these late coalescence events make up only a small proportion of the total dislocation density in the epilayers, the presence of dislocation bundles and
390 voids at these boundaries may mean that they have a disproportionate impact on the electrical properties of devices based on 3D/2D growth or other growth processes involving coalescence.

Acknowledgements

This work was supported by the European Research Council under the European Community's Seventh Framework Programme (FP7/2007–2013)/ERC Grant Agreement No. 279361 (MACONS) and by EPSRC
395 (Grant No. EP/M010589/1). The authors would like to thank Melanie Tribble for her assistance in the fabrication of lithographic markers.

References

1. Bennett, S. E. Dislocations and their reduction in GaN. *Mater. Sci. Technol.* **26**, 1017–1028
400 (2010).
2. Van Der Merwe, J. H. Crystal Interfaces. Part II. Finite Overgrowths. *J. Appl. Phys.* **34**, 123–127 (1963).
3. Matthews, J. W. Defects associated with the accommodation of misfit between crystals. *J. Vac. Sci. Technol.* **12**, 126 (1975).
405 4. Melton, W. A. & Pankove, J. I. GaN growth on sapphire. *J. Cryst. Growth* **178**, 168–173 (1997).
5. Ning, X. J., Chien, F. R., Pirouz, P., Yang, J. W. & Khan, M. A. Growth defects in GaN films on sapphire: The probable origin of threading dislocations. *J. Mater. Res.* **11**, 580–592 (1996).
6. Narayanan, V., Lorenz, K., Kim, W. & Mahajan, S. Origins of threading dislocations in GaN epitaxial layers grown on sapphire by metalorganic chemical vapor deposition. *Appl. Phys.*
410 *Lett.* **78**, 1544 (2001).
7. Oliver, R. A., Kappers, M. J. & Humphreys, C. J. Insights into the origin of threading dislocations in GaN/Al_2O_3 from atomic force microscopy. *Appl. Phys. Lett.* **89**, 011914 (2006).
8. Moram, M. A., Sadler, T. C., Häberlen, M., Kappers, M. J. & Humphreys, C. J. Dislocation movement in GaN films. *Appl. Phys. Lett.* **97**, 1–4 (2010).
415 9. Oliver, R. A. Application of highly silicon-doped marker layers in the investigation of unintentional doping in GaN on sapphire. *Ultramicroscopy* **111**, 73–8 (2010).
10. Massabuau, F. C.-P. *et al.* Correlations between the morphology and emission properties of trench defects in InGaN/GaN quantum wells. *J. Appl. Phys.* **113**, 073505 (2013).
11. Mancini, L. *et al.* Multi-microscopy study of the influence of stacking faults and three-
420 dimensional In distribution on the optical properties of m-plane InGaN quantum wells grown on microwire sidewalls. *Appl. Phys. Lett.* **108**, 042102 (2016).
12. Massabuau, F. C.-P. *et al.* Carrier localization in the vicinity of dislocations in InGaN. *J. Appl. Phys.* **121**, (2017).
13. Zhu, T. & Oliver, R. a. Unintentional doping in GaN. *Phys. Chem. Chem. Phys.* **14**, 9558 (2012).
425 14. Williams, C. C. TWO-DIMENSIONAL DOPANT PROFILING BY SCANNING CAPACITANCE MICROSCOPY. *Annu. Rev. Mater. Sci.* **29**, 471–504 (1999).
15. Sumner, J., Oliver, R. A., Kappers, M. J. & Humphreys, C. J. Practical issues in carrier-contrast imaging of GaN structures. *Phys. status solidi* **4**, 2576–2580 (2007).
16. Schubert, E. F., Goepfert, I. D., Grieshaber, W. & Redwing, J. M. Optical properties of Si-doped
430 GaN. *Appl. Phys. Lett.* **71**, 921 (1997).
17. Clarke, J. S., Schmidt, M. B. & Orji, N. G. Photoresist cross-sectioning with negligible damage using a dual-beam FIB-SEM: A high throughput method for profile imaging. *J. Vac. Sci.*

Technol. B Microelectron. Nanom. Struct. **25**, 2526 (2007).

18. Langford, R. M. & Petford-Long, A. K. Preparation of transmission electron microscopy cross-
435 section specimens using focused ion beam milling. *J. Vac. Sci. Technol. A Vacuum, Surfaces, Film.* **19**, 2186–2193 (2001).
19. Sumner, J. Scanning Probe Microscopy Studies on Gallium Nitride. (University of Cambridge, 2008).
20. Schaffer, M., Schaffer, B. & Ramasse, Q. Sample preparation for atomic-resolution STEM at
440 low voltages by FIB. *Ultramicroscopy* **114**, 62–71 (2012).
21. Uchic, M. D., Holzer, L., Inkson, B. J., Principe, E. L. & Munroe, P. Three-dimensional microstructural characterization using focused ion beam tomography. *MRS Bull.* **32**, 408–416 (2007).
22. Bassim, N. D., Stroud, R. M., Scott, K., Nittler, L. R. & Herd, C. D. Focused Ion Beam Slice-and-
445 View Tomography and Correlative Electron Microscopy of Multiphase Meteorite Particles. *Microsc. Microanal.* **19**, 870–871 (2013).
23. Jublot, M. & Texier, M. Sample preparation by focused ion beam micromachining for transmission electron microscopy imaging in front-view. *Micron* **56**, 63–67 (2014).
24. Oliver, R. A. Advances in AFM for the electrical characterization of semiconductors. *Reports*
450 *Prog. Phys.* **71**, 076501 (2008).
25. Massabuau, F. C.-P., Bruckbauer, J., Trager-Cowan, C. & Oliver, R. A. Microscopy of defects in semiconductors. in *Characterisation and Control of Defects in Semiconductors* 345–416 (Institution of Engineering and Technology, 2019). doi:10.1049/PBCS045E_ch8.
26. Wu, X. H. *et al.* Dislocation generation in GaN heteroepitaxy. *J. Cryst. Growth* **190**, 231–243
455 (1998).
27. Moram, M. A. *et al.* On the origin of threading dislocations in GaN films. *J. Appl. Phys.* **106**, 073513 (2009).
28. Narayanan, V., Lorenz, K., Kim, W. & Mahajan, S. Gallium nitride epitaxy on (0001) sapphire. *Philos. Mag. A* **82**, 885–912 (2002).
460 29. Matsubara, T., Sugimoto, K., Okada, N. & Tadatomo, K. Atomic-scale investigation of structural defects in GaN layer on c -plane sapphire substrate during initial growth stage. *Jpn. J. Appl. Phys.* **55**, 045501 (2016).
30. Cherns, D. & Liliental-Weber, Z. Can laterally overgrown GaN layers be free of structural defects? *GaN Relat. Alloy. - 2000. Symp. (Materials Res. Soc. Symp. Proc. Vol.639)* **639**, G5.2.1-
465 6 (2001).
31. Usami, S. *et al.* Effect of dislocations on the growth of p-type GaN and on the characteristics of p–n diodes. *Phys. Status Solidi Appl. Mater. Sci.* **214**, (2017).